Bioprinted Living Coral Microenvironments Mimicking Coral-Algal Symbiosis

Daniel Wangpraseurt,* Yazhi Sun, Shangting You, Sing-Teng Chua, Samantha K. Noel, Helena F. Willard, David B. Berry, Alexander M. Clifford, Sydney Plummer, Yi Xiang, Henry H. Hwang, Jaap Kaandorp, Julia M. Diaz, Todd C. La Jeunesse, Mathieu Pernice, Silvia Vignolini, Martin Tresguerres,* and Shaochen Chen*

The coral-algal symbiosis is the biological engine that drives one of the most spectacular structures on Earth: the coral reef. Here, living coral microhabitats are engineered using 3D bioprinting, as biomimetic model system of the coral-algal symbiosis. Various bioinks for the encapsulation of coral photosymbiotic microalgae (*Breviolum psygmophilum*) are developed and coral mass transfer phenomena are mimicked by 3D bioprinting coral tissue and skeleton microscale features. At the tissue–seawater interface, the biomimetic coral polyp and connective tissue structures successfully replicate the natural build-up of the O_2 diffusive boundary layer. Inside the bioprinted construct, coral-like microscale gastric cavities are engineered using a multi-material bioprinting process. Underneath the tissue, the constructs mimic the porous architecture of the coral aragonite skeleton at the micrometer scale, which can be manipulated to assess the effects of skeletal architecture on stress-related hydrogen peroxide (H_2O_2) production. The bioprinted living coral microhabitats replicate the diffusion-related phenomena that underlie the functioning and breakdown of the coral-algal symbiosis and can be exploited for the additive manufacturing of synthetic designer corals.

1. Introduction

Tropical coral reefs are hotspots of biodiversity and one of the most productive ecosystems on Earth. The evolutionary success of coral reefs and their existence in nutrient-poor environments is largely due to the highly efficient photosymbiosis between the coral host and their photosynthetic endosymbiotic dinoflagellate algae of the Symbiodiniaceae family. However, this photosymbiosis is very susceptible to environmental changes, including ocean warming, acidification, and nutrient enrichment.[1–3] Coral bleaching, which describes the paling of corals observed upon symbiosis breakdown,[4] is regarded as a major threat to the future existence of coral reefs.[3] The accelerating pace of coral bleaching events, combined with overfishing[5] and increased breakout of coral diseases, has resulted in the unprecedented loss of coral reefs worldwide.[3,6,7]

D. Wangpraseurt, Y. Sun, S. You, D. B. Berry, Y. Xiang, H. H. Hwang, S. Chen
Department of NanoEngineering
University of California San Diego
San Diego, CA 92093, USA
E-mail: dwangpraseurt@eng.ucsd.edu; chen168@eng.ucsd.edu
D. Wangpraseurt, S. K. Noel, A. M. Clifford, S. Plummer, J. M. Diaz, M. Tresguerres
Scripps Institution of Oceanography
University of California San Diego
San Diego, CA 92093, USA
E-mail: mtresguerres@ucsd.edu
S.-T. Chua, S. Vignolini
Bioinspired Photonics Group
Department of Chemistry
University of Cambridge
Cambridge CB2 1EW, UK

H. F. Willard, J. Kaandorp
Computational Science Lab
University of Amsterdam
Science Park 904, Amsterdam 1098XH, Netherlands
D. B. Berry
Department of Orthopaedic Surgery
University of California San Diego
San Diego, CA 92093, USA
T. C. La Jeunesse
Department of Biology
The Pennsylvania State University
University Park, PA 16802, USA
M. Pernice
Climate Change Cluster
University of Technology Sydney
Sydney, NSW 2007, Australia

ADVANCED
SCIENCE NEWS
www.advancedsciencenews.com

ADVANCED
FUNCTIONAL
MATERIALS
www.afm-journal.de

Worst-case predictions suggest that bleaching could be an annual event for the majority of coral reefs[8] ultimately leading to the degradation of a vast extent of global coral reefs by the end of this century.[9]

In addition to the direct environmental impacts, coral reef degradation entails serious repercussions for the economy of their associated coastal communities, due to potential catastrophic impacts on tourism, fisheries, and coastal protection from erosion.[10–12] While we urgently need to reduce carbon dioxide emissions to slow down coral degradation, scientists are concurrently exploring innovative and transformative approaches to restore coral reefs and improve their resilience.[13–15] Prominently, human-assisted evolution strategies propose infecting heat-resistant Symbiodiniaceae strains into coral hosts to reduce the likelihood of bleaching.[16] It is widely recognized that developing such approaches requires a detailed understanding of the processes that determine the functioning of the coral-algal symbiosis, and the factors that lead to its breakdown.[17–19] However, studying the natural coral-algal symbiosis has been hampered by the outstanding diversity and complexity of the coral holobiont, which describes the meta-association among the cnidarian animals, various Symbiodiniaceae strains,[20] and a complex microbial community.[21,22] Additionally, variations in coral macro- and micro-structural growth further affect many key biophysical parameters, including fluid flow, mass transfer, and light-matter interaction, thus highlighting the fine-tuned ecophysiology of corals.[15,23–25] Together, the combination of such biological and physical variability poses a significant challenge in identifying the general mechanistic principles governing both coral reef health and disease.

By enabling precise control over the spatial and temporal distribution of cells and extracellular matrix (ECM), 3D bioprinting can mimic the microenvironments of tissues and organs.[26] 3D bioprinting has revolutionized medical tissue engineering, stem cell research, regenerative therapy, and precision medicine[26–28] and our understanding of various diseases including cancer.[29] 3D bioprinting has also been used to engineer biomimetic living materials powered by microorganisms and is thus tailorable across a wide variety of applications, including biomedicine, bioenergy, living device fabrication, environmental applications, as well as model systems for complex natural systems.[30] Recently, bionic 3D printed corals have been fabricated for the cultivation of green microalgae for biomass and biofuel production.[31] The living coral-inspired photobioreactors mimicked the optical properties of natural corals which facilitated dense microalgal growth.[31]

Here, we aimed to develop 3D biomimetic living coral microhabitats for studying the functional aspects of the coral-algal symbiosis. Specifically, we developed a 3D bioprinting approach to mimic three different coral models hosting photosymbiotic algae. Each of these models mimicked one key structural property of natural corals: 1) a diffusive boundary layer (DBL) on top of the tissue; 2) a gastrovascular cavity within the tissue; and 3) a porous skeleton underneath the tissue (Figures S1–S3, Supporting Information). Our biomimetic corals allow for studying the diffusion-related phenomena that shape the coral-algal symbiosis and provide insights into distinct coral tissue microhabitats that control the physiology of their associated microorganisms. We provide a biological engineering perspective

to coral ecophysiology, thereby facilitating the development of next-generation biomaterials that can be exploited for reef restoration and other environmental engineering approaches in the future.

2. Results and Discussion

2.1. 3D Bioprinting of Coral Symbiont Bioink and Diffusive Boundary Layer Mimic

We developed a symbiont bioink to sustain the growth of the coral's native photosymbiotic algae. Initially, we tested a gelatin methacrylate (GelMA)-based bioink, due to the previous successful growth of green microalgae and its frequent application in tissue engineering (Figure S4, Supporting Information).[31,32] However, GelMA hydrogel scaffolds containing Symbiodiniaceae (*Breviolum psygmophilum*) showed visible signs of degradation and bacterial growth after just 7 days of cultivation. As most Symbiodiniacae strains are not axenic,[33] it is likely that gelatin facilitated the growth of associated bacterial communities (Figure S4, Supporting Information). We thereafter developed an alginate methacrylate (AlgMa)-based bioink that sustained robust growth and no visible bacterial degradation for about 2 weeks (see details in Experimental Section, Figure S5, Supporting Information).

Mass transfer of gases and metabolites is strongly affected by coral surface architecture, which controls the DBL buildup.[34] To mimic this microscale biophysical process, we bioprinted a mimic of the rough surface of the brain coral *Platygyra lamellina* (**Figure 1**A,B, Figure S2, Supporting Information). A digital-light processing (DLP)-based multi-step bioprinting approach allowed us to replicate the intricate coral surface architecture comprised of polyps and their interconnecting tissue ("coenosarc") (Figure 1A–C). This bioprinting approach rapidly constructed skeletal and tissue layers, resulting in large-scale (up to 1.5 cm) scaffolds. The short light exposure during printing (< 30 s) ensures minimal damage to the algal cells (cell viability > 95% after printing, Figure S6, Supporting Information) and facilitated the successful cultivation of *B. psygmophilum* (Figure 1D,E, Figure S5, Supporting Information). Similar to natural corals, the physical characteristics of the biomaterials used for the coral skeleton and coral tissue were designed to be different from each other (Figure S6, Supporting Information). To replicate the coral skeleton, we fabricated a strong hydrogel using poly(ethylene glycol) diacrylate (PEGDA), with a Young's modulus of $E = 17.4$ MPa (± 1.2 SD), which is comparable to natural coral skeletons ($\approx 9.5–14.5$ MPa)[35] (Figure S6, Supporting Information). In contrast, the coral tissue mimic was designed to be a soft hydrogel with a Young's modulus of $E = 2.3$ kPA (± 0.3SD) (Figure S6, Supporting Information).

This biomimetic coral was used to evaluate the effect of coral surface architecture on O_2 mass transfer under laminar flow conditions. 3D computational fluid models (CFD) predicted that O_2 is accumulated in the polyp, while it is rapidly exchanged over the coenosarc (**Figure 2**). O_2 microsensor measurements on the biomimetic coral revealed significant differences in coral mass transfer as the DBL thickness was about four-fold enhanced over the biomimetic polyp versus coenosarc
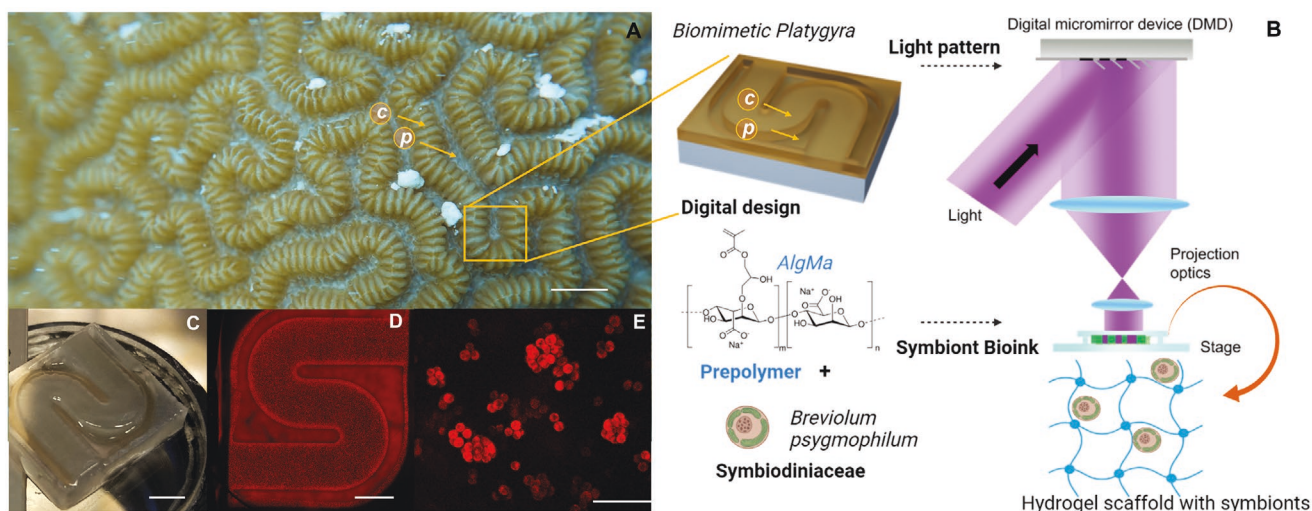
Figure 1. Biomimetic coral host printed to mimic coral mass transfer. A) Photograph of growth pattern and microscale architecture of the brain coral (*Platygyra lamellina*) growing on the Heron Island Reef Flat, Great Barrier Reef, Australia (Photo: D. W.). Scale bar = 4 mm. Connective tissue (coenosarc, *c*) and polyp tissue (*p*). B) DLP-based bioprinting approach. A digital schematic of an engineered model of biomimetic brain coral, as well as the structural formula diagram of symbiont bioink. A custom-made bioprinter polymerizes a hydrogel scaffold with photosymbionts. C) Bioprinted scaffold visualizing the tissue and underlying skeletal mimic immediately after printing. Scale bar = 2 mm. D) Chlorophyll *a* fluorescence image of 7 day-old encapsulated *Breviolum psygmophilum*. Scale bar = 2 mm. E) Magnified image of the same scaffold depicted in D) showing *B. psygmophilum* aggregates in the host tissue mimics. Scale bar = 50 μm.

(ANOVA, $F_{1,23}$ = 219.8, $p < 0.01$; Figure 2D). Likewise, microsensors measured significantly enhanced O_2 microhabitats for polyp versus coenosarc tissues, yielding about 1.5 fold differences at day 7 ($\approx$402 ±16.7 μM vs 278 ±1.4 μM polyp and coenosarc, respectively, ANOVA $F_{1,13}$ = 35.86, $p < 0.01$, Figure 2D). These values are comparable to what has been measured in massive corals exposed to comparable irradiances in nature.[34,36] Additionally, because of the thick DBL over the biomimetic polyp, O_2 fluctuations between light-dark transitions are more extreme compared to O_2 conditions over the coenosarc (Figure S7, Supporting Information), suggesting a more dynamic microenvironment. Our results clearly exemplify the substantial impact that microscale architectural heterogeneity can have on chemical microenvironments across the coral surface, which are bound to shape the cellular physiology of both the coral host cells and that of their associated microbes.[37] The photophysiological activity of encapsulated *B. psygmophilum* reflected the microenvironmental heterogeneity of the biomimetic 3D printed coral. Photosynthetic O_2 production rates were up to $\approx$50% lower in the polyp mimic area than in the coenosarc mimic area (Figure 2F), most likely due to the limitation of photosynthesis imposed by decreased O_2 efflux due to mass transfer resistance and decreased CO_2 influx towards the algae.[38,39]

2.2. 3D Bioprinting of Gastrovascular Cavity Mimic

Coral tissues consist of the oral epidermis and gastrodermis towards the tissue surface, and the aboral gastrodermis and calicodermis towards the skeletal surface (Figure S1B, Supporting Information). The oral and aboral tissue layers are separated from each other by the gastrovascular cavity, which circulates a seawater-like fluid throughout the coral colony (Figure S1B,

Supporting Information). As a result of metabolic activity, the chemistry of the gastrovascular fluid is very different from that of environmental seawater.[40,41] The Symbiodiniaceae algae are hosted in the oral and aboral gastrodermis; however, algal density and photophysiology can greatly vary among different regions of the coral tissue.[42,43] As a first step towards the bioprinting of different coral tissue layers and a gastrovascular cavity, we developed a multi-layer, multi-material bioprinting approach (**Figure 3**A). *B. psygmophilum* was encapsulated in AlgMa-based bioink for oral and aboral tissue layers, while glycidyl methacrylate hyaluronic acid (GM-HA)[44] was printed in the location of the gastrovascular cavity as a temporary sacrificial material, which was subsequently dissolved using hyaluronidase.[45] The gastrovascular cavity mimic was 750 μm in diameter, which is similar to what can be found in an expanded coral tissue[46] (Figure S2, Supporting Information).

After 7 days of cultivation in the biomimetic coral, *B. psygmophilum* cells grew to large aggregates reaching a maximal cross-sectional area of about 350 μm (Figure 3E,F). Overall, aggregate size was similar between locations and treatments but there was a trend toward improved growth in aboral tissue layers relative to oral tissue layers when gastric cavities were present compared to the control treatment (i.e., cavities filled with inert PEGDA, see methods, Figure 3F and Table S1, Supporting Information, aboral cavity mean = 285 μm^2 vs aboral control mean = 243 μm^2). Likewise, the flow slightly reduced the mean aggregate size (302 μm^2 ±165 SD vs 283 μm^2 ±156 SD, Figure 3F,G). Although our focus was on developing new tools to study coral-algal symbiosis, these observations suggest that encapsulated photosymbionts benefit from the improved gas exchange in the presence of the gastric cavity. In nature, the coral tissue structure is dynamic, as corals are able to modulate the tissue volume in response to changes in flow velocity and irradiance.[47–49] Such dynamic coral microenvironments could
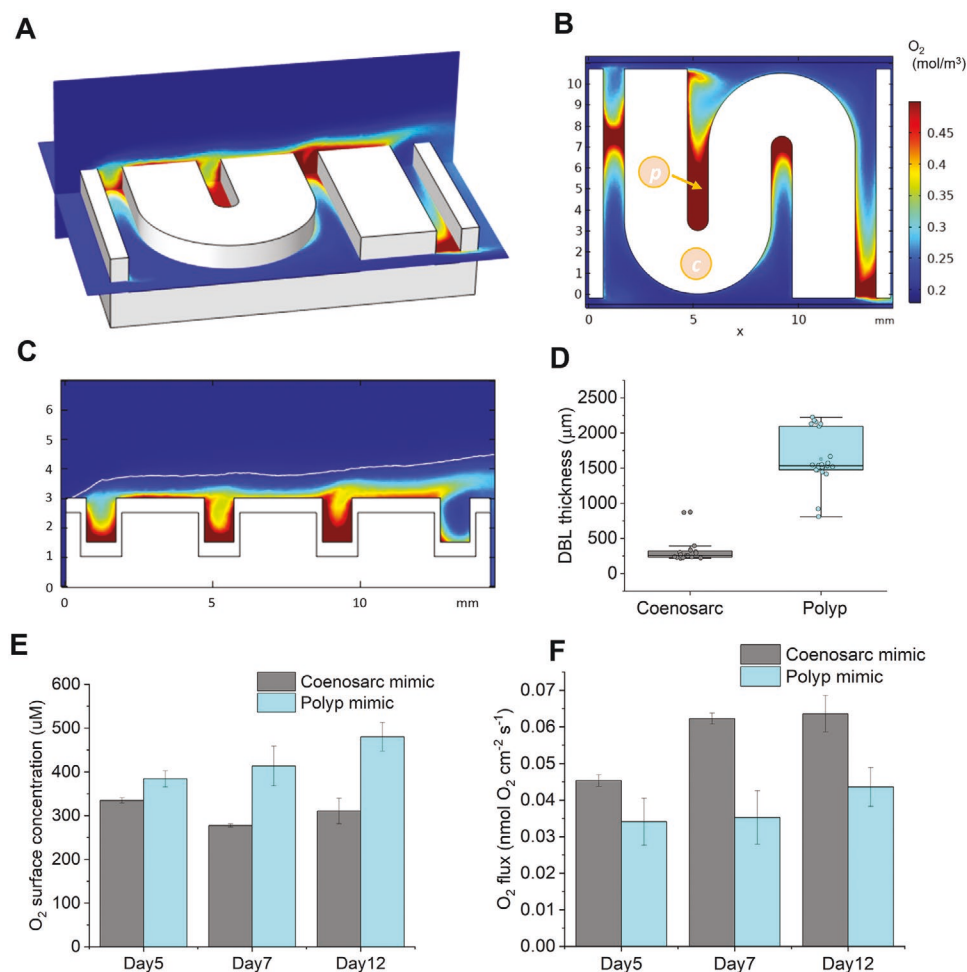
**ADVANCED
SCIENCE NEWS**
www.advancedsciencenews.com

**ADVANCED
FUNCTIONAL
MATERIALS**
www.afm-journal.de

Figure 2. O_2 microhabitats and mass transfer of biomimetic brain coral. A–C) Computational fluid dynamics models of O_2 exchange. A) 3D model showing the O_2 distribution on the x–y plane at $z = 2$ mm and x–z plane at $y = 7$ mm. B) Top view of z plane ($z = 2$ mm) indicating O_2 build-up over the polyp tissue. C) Side view (x–z plane = 7 mm) visualizing the thickness of the DBL (white line, i.e., $O_2 = 0.21$ mM). D–F) O_2 microsensor measurements on bioprinted scaffolds, showing the D) DBL thickness ($n = 10$–15), E) O_2 surface concentration ($n = 4$–9) and F) net photosynthesis ($n = 4$–9) (O_2 flux). Data are means ±SEM (panels E and F).

be manufactured via 4D bioprinting of shapeshifting materials in future studies.[50]

2.3. 3D Bioprinting of Internal Coral Skeletal Architecture

The biophysical control of the coral host extends beyond the tissue surface as the internal architecture of the coral skeleton is intricate, resulting in unique physicochemical characteristics (**Figure 4**A,B) that affect the ecophysiology of the coral-algal symbiosis, as well as that of their endolithic communities.[42,51] Many massive corals (e.g., of the family Faviidae and Merulinidae) have large skeletal porous spaces; however, other coral species (e.g., pocilloporids) have more solid aragonite skeletons.[42,52] The potential effects of these dissimilar skeletal architectures on mass transfer and consequently coral physiology remain largely unexplored,[53] partially due to methodological challenges.

We sought to address these challenges by 3D printing porous coral skeleton mimics. To build the skeleton mimic, we first generated a digital mask of the highly porous internal skeletal architecture of *P. lamellina* using micro-computed tomography (µCT) images as reference (Figure 4A–C). DLP-based printing was used to replicate the skeletal pores (≈100 µm width). Since this approach can generate a maximal x–y resolution of about 2.5 µm,[54] the pore spaces of the 3D printed mimic were in good agreement with those of the natural coral skeleton (average structural similarity index = 0.66, where 1 = perfect geometric agreement between model and printed structure and −1 = no structural similarity[55]). We used this biomimetic coral skeleton to explore the effect of porosity on the production of hydrogen peroxide (H_2O_2), one of the main reactive oxygen species (ROS) in corals. Indeed, oxidative stress has been proposed as the main factor that triggers coral bleaching.[56] ROS production generally correlates to O_2 concentration in biological systems,[57] and computational simulations revealed that skeletal porosity reduces the O_2 concentration in coral tissues by enhancing mass transfer (Figure S8, Supporting Information). We thus hypothesized that skeletal pores would lower ROS production in coral tissues compared to solid skeletons without
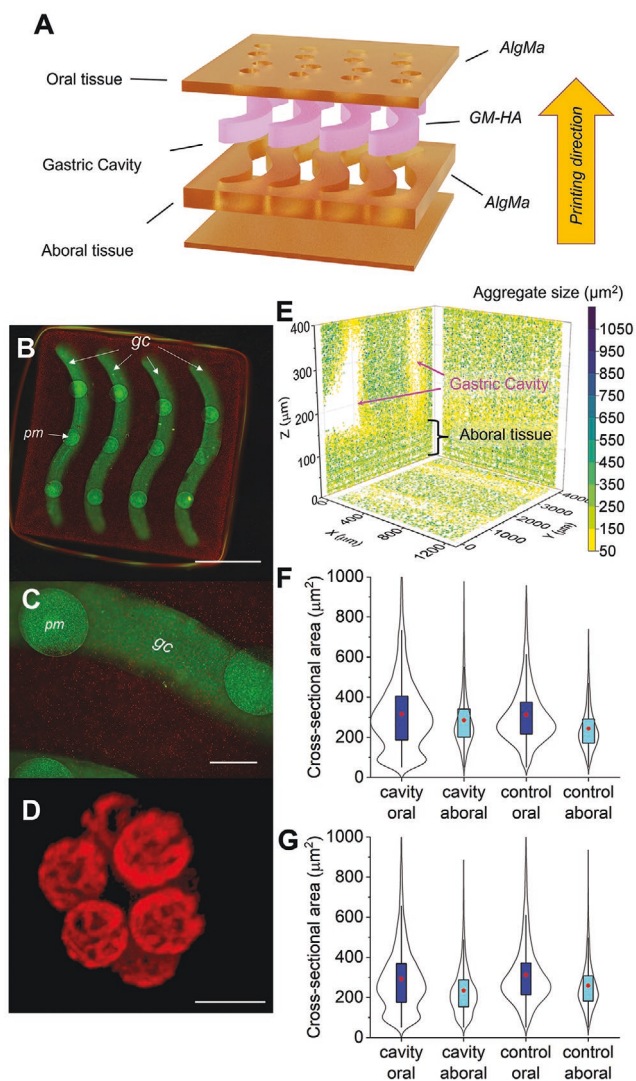
Figure 3. 3D Bioprinting of coral gastric cavity. A) Exploded schematic of the multi-material printing approach used. GM-HA was utilized as a sacrificial bioink, whereby their occupying space was developed into the gastric cavity following enzymatic degradation via hyaluronidase. The oral and aboral tissues were printed using AlgMA bioink containing *Breviolum psygmophilum*. B) Fluorescent image overview of printed scaffold showing chlorophyll *a* fluorescence of *B. psygmophilum* (red) and fluorescent spheres (green) used to visualize the distribution of the gastric cavity (*gc*). Round circles (pm) are polyp mouth openings. Scale bar = 3 mm. C) Close-up image of the gastric cavity (scale bar = 500 µm) and D) close-up image of individual *B. psygmophilum* aggregate (scale bar = 10 µm). E) Representative 3D plot of analyzed and segmented algal aggregates (based on chlorophyll *a* fluorescence) of 7-day old scaffold grown under ambient flow. The color map indicates the aggregate cross-sectional area (µm²). F,G) Violin plots showing the distribution of aggregate size for scaffolds with gastric cavity versus control treatments (channels filled with PEGDA). Analysis was performed for oral (200 µm thick, dark blue) and aboral (100 µm thick, turquoise) tissues in the presence of F) flow and G) under stagnant conditions.

pores. To test this, we developed a three-step printing approach, where algal-containing tissues and the skeleton (either porous or solid) are printed separately and attached to each other with a small volume (15 µL) of algal-free AlgMA as a functional

adhesive, to prevent tissue polymerization within the skeletal scaffold (Figure 4).

Our results showed that ROS production in porous skeleton mimics decreased by 40% compared to solid skeleton mimics (ANOVA, $F_{1,10} = 42.1$ $p < 0.01$, Figure 4H), suggesting that chemical diffusion through skeletal pores is an important and potentially overlooked mechanism in coral ecophysiology. In nature, the coral skeletal microhabitat is further affected by the endolithic community that lives inside the skeleton,[42,51] which will generate local chemical microhabitats by respiration and photosynthesis that could affect the coral host via diffusion through the skeletal pores (Figures S1 and S9, Supporting Information). Our bioprinting approach provides an experimental means to study these spatial interactions in a controlled manner for a range of massive and branching corals (Figure 4, Figures S10 and S11, Supporting Information) with different porosities.

3. Conclusion

In conclusion, we have fabricated living coral microhabitats that mimic distinct structural properties and key diffusion-related processes of the coral-algal photosymbiosis. The living bioprinted tissue microhabitats were constructed with a symbiont bioink which facilitated the growth and photosynthesis of coral photosymbionts. Our 3D bioprinting approach mimicked coral mass transfer and the build-up of DBLs, highlighting the importance of coral microtopography in structuring the chemical microenvironment of corals. Multi-material bioprinting enabled successful replication of the coral gastric cavities and this approach can now be exploited to study the role of coral intra-tissue gas exchange and waste transport. The biomimetic coral skeleton provides an experimental tool to study the interaction between skeletal microhabitat and coral physiology, facilitating the controlled encapsulation of microorganisms. Our programmable materials are customizable for studying the role of a plethora of coral skeletal designs on coral health. Future studies will also be able to encapsulate different Symbiodiniaceae strains or synthetic consortia in such biomimetic coral microenvironments, enabling a mechanistic understanding of complex host-microbe interactions. Additionally, such microscale bioprinted living materials could be combined with larger-scale 3D printing approaches aimed at coral reef restoration.[58,59] We anticipate that the fabricated living coral microenvironments will find wide applications in coral reef science and will be further developed as a next-generation technology for coral stress and bleaching studies, ultimately paving the way for the engineering of novel biomaterials and artificial coral reefs.

4. Experimental Section

Diffusive Boundary Layer Mimic: To mimic the physicochemical microhabitat of natural corals, the mass transfer dynamics was mimicked by recreating the DBL properties of natural corals.[34,60] Often strong differences in mass transfer existed between different coral compartments. For instance, there were stark differences in DBL thickness between polyp and coenosarc tissues of massive
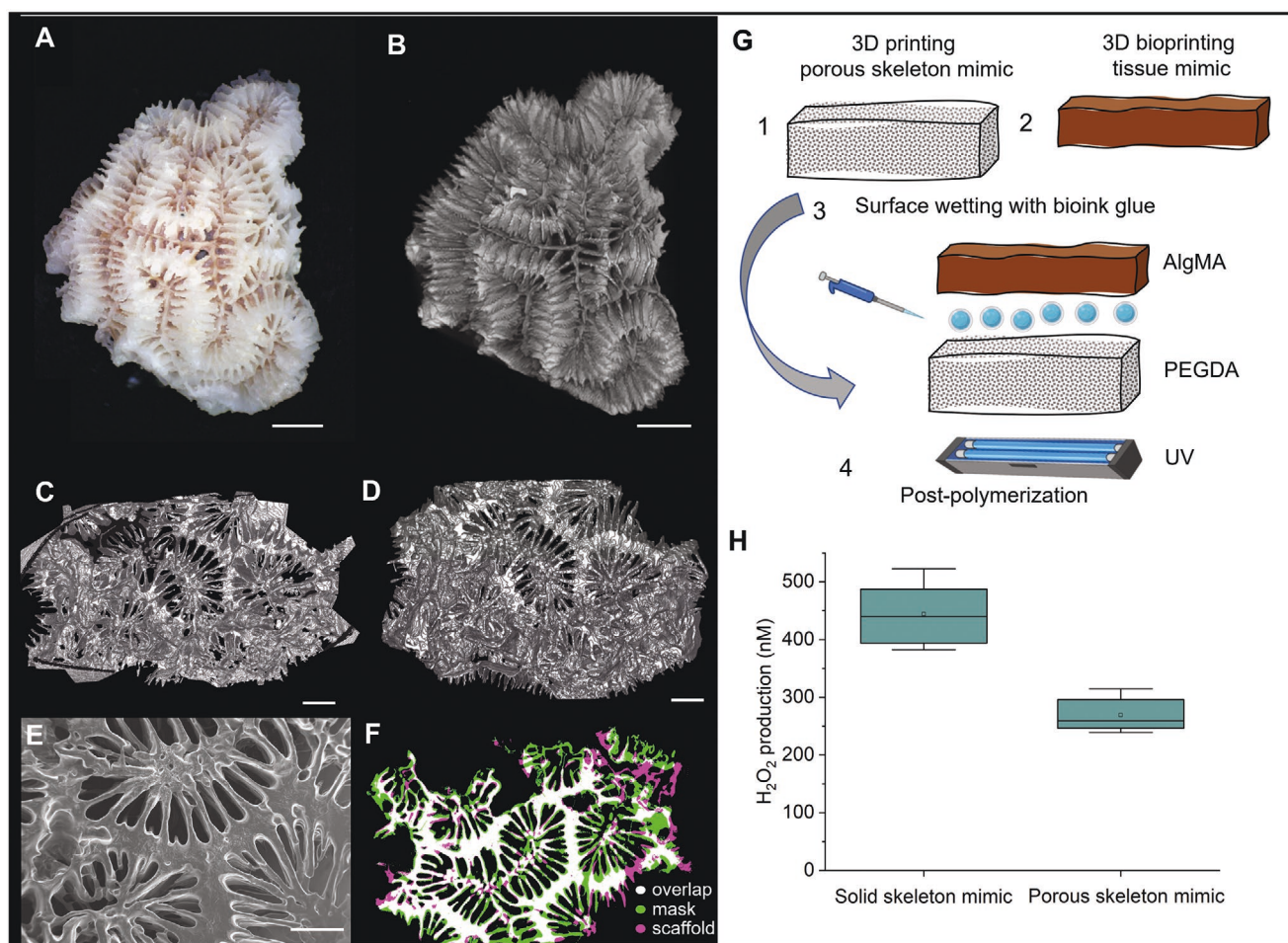
**ADVANCED
SCIENCE NEWS**

www.advancedsciencenews.com

**ADVANCED
FUNCTIONAL
MATERIALS**

www.afm-journal.de

Figure 4. Biomimetic coral skeleton. A) Close-up image of the natural coral skeleton of *Platygyra lamellina* and B) surface view of rendered μCT images of the same coral fragment. C) μCT of inner parts of the porous skeleton of the natural coral and D) of the 3D printed mimic. E) Example SEM scan of the 3D printed mimic, showing the highly porous skeletal architecture. F) Structural similarity analysis of registered μCT images of real coral (mask, green) and 3D printed mimic (scaffold, purple) as well as the overlap between them (white). Scale bars are 4 mm (panel A,B), 2.5 mm (panel C,D) and 2 mm (panel E). G) Bioprinting approach to test the role of skeletal porosity on ROS evolution of Symbiodiniaceae. H) Box plot H_2O_2 production for algae on top of a solid skeleton versus a porous skeleton mimic ($n = 6$ printed scaffolds).

corals of the family Faviidae due to the heterogenous coral surface skeleton architecture (i.e., corallite vs coenosetum).[61] To mimic such microstructurally-induced differences in coral gas exchange, a 3D bioprinted mimic of the massive coral species *P. lamellina* was developed. Skeletal designs were based on μCT scanning (details below) and tissue designs were approximated based on previous anatomical observations of tissue thickness[46] (Figure S2, Supporting Information). As the primary aim was to mimic the DBL between corallite and coenosteum, the tissue followed the skeletal architecture over the polyp and coenosarc areas but omitted any further heterogeneities of the coenosarc tissue and used a simplified smoothed tissue surface (Figure S2, Supporting Information). This is because the DBL was not affected by such minor topographic features of the coral tissue, and smooth features that were roughly < ½ DBL thickness.[62,63] Source architectures for bioprinting were designed in AutoCAD (Autodesk, USA) and sliced for 3D printing using a custom-written MATLAB code.

Gastrovascular Cavity Mimic: Corals have a diploblastic tissue arrangement with an oral and aboral tissue layer and a gastrovascular cavity in between. The cavity had been proposed to be responsible for gas exchange as well as the proliferation of gastric fluid and zooxanthellae. To develop a gastrovascular cavity, channels averaging 750 μm in diameter and connected to a polyp opening (1 mm in diameter) were

designed.[46] The oral tissue was 200 μm in thickness and the aboral tissue was 100 μm in thickness. Gastrovascular channels were separated laterally by 1 mm in spacing.

Bioprinters: Bioprinting was performed using the in-house built 3D bioprinter,[31,64] which consisted of a 385 nm LED light source, focusing optics, a digital micromirror device (DMD) chip (Texas Instruments, USA), a building platform, and a three-axis controllable stage (Zaber, Canada). The DMD chip was composed of over 4 million micromirrors (in a 2560 × 1600 micromirror array), and each micromirror could be digitally controlled to turn on or off to project designed masks. The printer was connected to a computer with custom-written software for digital mask input and building platform movement control. During printing, the 3D model was sliced into multiple cross-sections by the software, and the cross-sections were loaded on the DMD sequentially. The LED light was modulated by the DMD, and thus the cross-section patterns were projected onto the photocurable bioink. A thin layer of bioink could be crosslinked within a few seconds to a few tens of seconds of exposure. After exposure, the motorized stage lifted the cured sample by a layer's thickness, allowing the uncured bioink to refill the gap between the cured sample and the substrate. Next, a new layer was formed by the exposure of the next cross-section. By repeating this process, the 3D object was fabricated.

With the help of the optical system, the fabrication resolution of the 3D bioprinter was 3 microns. Since this DMD projection method could fabricate an entire layer with one exposure, it was much faster than other raster-scanning style 3D printing techniques such as ink-jet-based 3D printing, extrusion-based 3D printing, and stereolithography. Hence, this bioprinting technique was a promising tool for high-resolution, high-throughput biomanufacturing.

3D Bioprinting of DBL Mimic: To print the DBL mimic, a multi-material printing process was developed. To print the skeleton mimics, PEGDA (Mn = 6000) was first used. However, because the multi-step printing process required several material exchanges (followed by washing and air drying), the dehydration of the scaffold induced slight surface shrinkage and a detachment of the scaffold from the building platform. To overcome this, the bioink was optimized and used 50% PEGDA (Mn = 700) and 50% deionized (DI) water that was doped with a low concentration of cellulose nanocrystals (CNC) at a final concentration of 2%.[31] No detachment effect was observed using this bioink, presumably due to reduced dehydration when adding CNC (Figure S6, Supporting Information). For the soft coral tissue mimic, an AlgMa-based bioink was developed (Figure S6, see details in Polymer Synthesis below). Multi-material printing was performed by washing and air drying the printed scaffold between bioink change steps.

3D Bioprinting of Gastrovascular Cavity Mimic: To print the aboral coral tissue mimic, a methacrylated coverslip was glued to the printing probe using UV glue. The AlgMA bioink was loaded on a PDMS coated plate providing a non-stick surface. The plate was placed at the height of the focus plane. Photopolymerization occurred at a fixed height and the pre-polymer filled the gap between the probe and the plate due to capillary forces. In this setting, photo-crosslinked AlgMA was preferentially bound to the methacrylated coverslip through covalent bonding, thus having a long-term stable attachment. Next, the gastrovascular channels were printed using GM-HA, which is often used as a sacrificial tissue (e.g., to induce pre-vascularization), due to its rapid enzymatic degradation as induced by hyaluronidase.[45] Between each tissue layer, the remaining pre-polymers were removed by washing it with a cultivation medium followed by air drying in a laminar flow chamber. Lastly, the oral tissue layer was printed using the same AlgMA bioink as for the aboral tissue. 3D bioprinted scaffolds were carefully removed from the imaging probe using a razor blade and scaffolds were placed in a six-well plate with 3 mL 5% v/v f/2 medium in each well. Hyaluronidase (Stemcell Technologies, USA) was added at a final concentration of 300 units mL^{-1} cultivation medium to each well following printing. Scaffolds were incubated for 24 h at 25 °C in static conditions, after which the GM-HA layer for supporting channels was fully dissolved by hyaluronidase. Following enzymatic degradation, the medium was replaced with a standard cultivation medium (5% v/v f/2 medium).

3D Bioprinting of Porous Skeleton and Tissue Mimic: Based on the µCT of coral skeletons, a digital mask that is used for pore space printing was created. Printing was performed using a bioink formulated from PEGDA (Mn = 700) and yellow food dye (0.1% v/v, Wilton Candy Colors, USA) as a photoabsorber. Microscale photopolymerization was done by the continuous movement of the motorized stage of the bioprinter synchronized with the projected digital mask to create smooth 3D constructs without interfacial artifacts. The skeleton mimic was washed with isopropyl alcohol, dried, washed with DI water, and dried again. To test the relevance of such skeletal pore spaces for coral physiology, the living tissue mimic on top of the skeleton was printed. To ensure that no pre-polymers filled the internal space, the tissue mimic and skeleton were printed separately and later combined the two layers using post-polymerization (30 s) with a small volume (15 µL) of algal-free AlgMa prepolymer under a laminar flow hood. This method resulted in stable scaffolds and no detachment was observed even after strong agitation. The tissue was printed to be 1 mm thick using the same AlgMa-based bioink, and a final concentration of *B. psygmophilum* cells of 5.5×10^6 cells mL^{-1}. The same method was used to print control scaffolds that consisted of a solid slab of PEGDA instead of the porous skeleton mimic with solid skeletons. Following printing, scaffolds were placed in six-well plates and allowed to acclimate overnight before ROS measurements were performed (see below).

Symbiodiniaceae Stock Culture Cultivation: *B. psygmophilum* (Purpflex) cultures were grown in the f/2 medium[65] supplemented with antibiotics (pen/strep 1:1000, kanamycin 1:1000[66]) in sterile culture flasks at 25 °C controlled by a growth incubator (model: MIR-154, PHCbi, UK). The incident downwelling irradiance was ≈100 µmol m^{-2} s^{-1} photons, provided by white LED light panels (AL-H36DS, Ray2, Finnex) in a 12/12 h photoperiod. For bioprinting experiments, stock cultures were sampled during the active growth phase (about 3–5 days after subculturing). Cells were sampled and if needed spun down at a low centrifugal force of 200 rcf for 3 min to achieve a desired seeding cell density.

Bioprinted Scaffold Cultivation: Bioprinted scaffolds were grown in a similar manner to stock cultures (25 °C, ≈100 µmol m^{-2} s^{-1} photons downwelling irradiance; in a 12/12 h photoperiod). To reduce bacterial growth during scaffold cultivation, the f/2 medium with lowered nutrient concentrations (0.04 mmol NaNO$_3$, 0.002 mmol NaH$_2$PO$_4$) was used and supplemented with antibiotics (penicillin 100 units mL^{-1}, streptomycin 50 µg mL^{-1}, kanamycin 50 µg mL^{-1}). Scaffolds were grown in petri-dishes with either low turbulent flow induced by a magnetic stirrer bar (at 200 rpm, not in physical contact with the scaffolds) or under stagnant conditions.

Cell Viability: Cell viability in liquid cultures prior to 3D bioprinting and in hydrogels after printing was assessed via trypan (Sigma T8154) blue live/dead staining.[67] For liquid cultures, trypan blue was diluted with culture media (50% v/v); which was passed through a 0.22 µm filter, and the resultant solution was added to liquid culture media in a 1:5 ratio.[67] Cell viability was immediately assessed via hemocytometer counting. For scaffolded cultures, the bathing media was drawn off scaffolds and then incubated with the trypan blue mixture (50% v/v) for 10 min. Scaffolds were thereafter rinsed three times with media.[68] Four printed scaffolds were imaged and for each scaffold 10 technical replicate images were taken under a 10x objective. Images were manually counted for cell viability.

Polymer Synthesis: Poly(ethylene) glycol diacrylate (PEGDA, Mn = 700 Da and Mn = 6000 Da) was purchased from Millipore-Sigma (St. Louis, MO). Alginate methacrylate (AlgMA) was synthesized as previously described.[69] Briefly, AlgMA was synthesized in a 0.5M sodium chloride solution buffered by 50 mM 2-morpholinoethanesulfonic acid with a pH of 6.5 at room temperature. Sodium alginate with low viscosity was dissolved at 1% (w/v). To each gram of sodium alginate, 2.3 mmol N-hydroxysuccinimide (NHS) and 4.6 mmol 1-ethyl-3-(3-dimethylaminopropyl)-carbodiimide hydrochloride (EDC) were added to activate the carboxylic acid groups for 5 min. Subsequently, 2.3 mmol 2-aminoethyl methacrylate hydrochloride per 1 g sodium alginate was added, and the reaction was maintained for 24 h. The reaction was aborted by precipitating the mixture with excessive acetone. The precipitation was rehydrated with MilliQ water to 1%(w/v) and purified by dialysis against MilliQ water for 7 d using 3.5 kDa cutoff dialysis tubing. The solution was lyophilized and the product was stored at −80 °C. For bioink preparation, lyophilized AlgMA was dissolved in the f/2 medium (without nutrients) to create a 3% w/v stock solution. The final AlgMA bioink was prepared by mixing AlgMA stock solution, photoinitiator LAP, and cell solution with the composition of 2% w/v AlgMA and 0.5% w/v LAP and *B. psygmophilum* cells (3.3×10^6 cells mL^{-1}) for DBL mimicry experiments.

Gelatin methacrylate (GelMA) was synthesized as described previously.[31] Briefly porcine gelatin (Sigma Aldrich, St. Louis, MO, USA) was mixed at 10% (w/v) into the f/2 medium (without nutrients) and stirred at 60 °C until fully dissolved.[31,70] Methacrylic anhydride (MA; Sigma) was added until a concentration of 8% (v/v) of MA was achieved. The reaction continued for 3 h at 60 °C under constant stirring. The solution was then dialyzed against distilled water using 12–14 kDa cutoff dialysis tubing (Spectrum Laboratories, Rancho Dominguez, CA, USA) for 7 days at 40 °C to remove any unreacted methacrylic groups from the solution. The GelMA was lyophilized at −80 °C in a freeze dryer (Freezone, Labonco) for 1 week to remove the solvent.

GM-HA was prepared as described previously.[44] Briefly, 1 g of HA was dissolved in 100 ml of 50% acetone solution at room temperature overnight. Then, 7.2 ml triethylamine (Sigma) and 7.2 ml GM (Sigma) were added dropwise until fully mixed. The solution was stirred at room temperature overnight, then dialyzed against DI water with 3.5 kDa dialysis tubing (Spectrum Labs) for 48 h. The DI water was changed at 2, 4, 12, and 24 h. The GM-HA solution was lyophilized at −80 °C in a freeze dryer (Freezone, Labonco) for one week to remove the solvent. The GM-HA printing solution for mimicking gastric channels was prepared by mixing a 5% w/v stock solution and DI water to reach 1% w/v final concentration for printing.

The photoinitiator lithium phenyl-2,4,6 trimethylbenzoylphosphinate (LAP) was synthesized as described previously.[31] First, 2,4,6-trimetyhlbenzoyl chloride (Sigma-Aldrich) was added to an equimolar amount of dimethyl phenylphosphonite (0.018 mol, Acros Organics) at room temperature and under argon.[71] The mixture was stirred for 18 h after which 6.1 g lithium bromide was added to 100 mL of 2-butanone. The mixture was heated to 50 °C for 10 min and the precipitate was filtered with 2-butonone under vacuum. LAP was freeze-dried and stored for further use. The photoinitiator Irgacure 819 was purchased from BASF.

Cellulose nanocrystals were prepared as described previously.[31] Briefly, suspensions were prepared from the hydrolysis of Whatman cellulose filter paper (No.1) with sulfuric acid (64 wt %), prior to quenching with ice water (Milli-Q). The solution was centrifuged (20000×g) for 20 min and dialyzed against DI water (MWCO 12–14 kDa membrane). Any residues were removed. The suspension was tip-sonicated in an ice bath (Fisher Ultrasonic) and vacuum-filtered using a nitrocellulose filter (8.0 µm then 0.8 µm pore size, Sigma-Aldrich) followed by evaporation under ambient water.

Physical Characterization of Hydrogels: The elastic modulus for PEGDA and AlgMa hydrogels was measured with a microscale mechanical strength tester (Microsquisher, CellScale) as described previously.[72] Cylinder hydrogel scaffolds (1mm in diameter and 1 mm in height) were printed using the same light exposure parameters as for the biomimetic coral. Samples were compressed by a platen adhered to a cantilever at a rate of 3 µm s^{-1} to reach a displacement of 180 µm, held for 2 s, and then allowed to recover at a rate of 9 µm s^{-1}. The compression and relaxation process was performed three times and the force and displacement were recorded. To remove the effect of hysteresis, the third compression was used to calculate the modulus of the sample. The resulting stress-strain curves were calculated by measuring the slope of each curve in its elastic region using a custom-written MATLAB script.[72]

The stability of the PEGDA and AlgMA constructs was further evaluated by determining the swelling ratio.[72] Briefly, printed slabs were incubated in cultivation media in six-well plates at an experimental temperature (25 °C). Scaffolds were imaged on day 1 (24 h after printing), day 3, and day 7 using a Leica DMI 6000-B microscope to obtain the hydrated cross-sectional area (A_{wet}). Thereafter, scaffolds were washed with DI water and dried in the oven (at 37 °C) for 3 days. Imaging was performed on the dried scaffolds to determine the cross-sectional dry area (A_{dry}). Normalizing A_{wet}/A_{dry} calculated the swelling ratio. All image analysis was performed in ImageJ. While this method worked well for PEGDA scaffolds, slow drying of the soft AlgMA constructs resulted in stretching of the liquid meniscus and flattened the scaffold (i.e., increase in surface area, SA). Therefore, to characterize any physical differences in printed versus swollen samples, the % change in SA for day 1, day 3, and day 7 relative to the expected SA was calculated, as determined by the digital mask. These results revealed only minor differences between expected SA and printed SA for the duration of the experiment (Figure S6, Supporting Information).

Micro Computed Tomography Imaging: Natural coral skeletons as well as the 3D printed samples were analyzed using a Skyscan 1076 µCT scanner (Bruker, Kontich, Belgium). To improve scanning resolution and remove any debris, natural coral skeletons were thoroughly cleaned and soaked for 4 h in sodium hypochlorite. Skeletons were dried for 48 h at 60 °C.[73] Samples were mounted horizontally and scanned at 9 × 9 × 9 µm voxel size, applying an electrical potential of 50 kVp, a current of 200 µA, 180° in 0.8° steps, and using a 0.5 mm Al filter. All µCT image processing was performed using MATLAB (MathWorks, Natick, MA). First, 3D models of coral geometry were generated using imbinarize. These models were then reformatted to generate masks for DMD-based 3D printing using imresize3. In order to quantitatively compare the geometric structure between 3D printed and native corals, scaffolds with coral informed geometry were additionally printed and scanned using µCT (Figure 4F, Figure S11, Supporting Information).

Fluorescence Microscopy Imaging: To evaluate the growth and distribution of Symbiodiniaceae cells across the entire scaffolds, a fluorescence microscope (BZ-X800E, Keyence, USA) was used. Chlorophyll *a* fluorescence imaging was performed using fluorescent filters (Texas Red, Excitation 560/40 Emission 630/75) at 5x or 10x magnification across the scaffold. Serial images were aligned using the automated stitching function of the manufacturer's software.

To characterize individual algal cells and aggregates at high resolution, imaging was performed using a super-resolution confocal microscope (Zeiss LSM 800 with Airyscan). Bioprints from the DBL mimicry experiment were imaged upside down in glass-bottom microwell dishes (Mattek, USA). While the coenosarc mimics were easily accessible, it was not possible to focus on the tissue areas of the polyp mimics when the scaffold was intact. Thus, the coenosarc areas were carefully removed with a sharp scalpel to get a flat surface that was in direct contact with the glass of the microwell dish. For each confocal scan, imaging was performed at 20x or 40x using a 650 HE laser as excitation and the in-built chlorophyll *a* filter set-up. Z-stacking was performed with vertical step sizes of 3–6 µm. For the gastrovascular cavity experiment, imaging was performed as described above. However, because only soft tissue was printed, it was possible to image directly from the top (i.e., oral tissue) and the bottom (i.e., aboral tissue). No sectioning was needed. To get a better overview of channel distribution, z-stacks were aligned in x–y using the automated stitching function of the software (Zen 2.6 [blue edition], Carl Zeiss Microscopy GmbH, Germany).

Microsensor Measurements: Clark-type O$_2$ microsensors (tip size 25–50 µm, Unisense, Aarhus, Denmark) were used to measure O$_2$ microenvironments and photosynthesis of the 3D bioprinted scaffolds. Measurements were performed as described previously.[31,74] Briefly, sensors were mounted to a motorized micromanipulator (MU1, Pyroscience GmbH, Germany) that was attached to a vibration-free optical table. Bioprints were placed in a custom-made laminar flow system that provided slow laminar flow (flow rate = 1 cm s^{-1}). Illumination was provided at defined levels of incident downwelling irradiance (130 µmol m^{-2} s^{-1} photons) by a fiber optic halogen light source (ACE, Schott GmbH). O$_2$ profiles were performed on three experimental days (days 5, 7, and 12). Preliminary measurements were performed on earlier experimental days as well but did not show substantial O$_2$ production due to the low cell density. For each experimental day, 2–3 scaffolds were measured for each treatment (flow vs stagnant), and on each scaffold 2–3 replicate profiles were measured for each location (polyp vs coenosarc). Measurements over the biomimetic polyp were restricted to the polyp pockets, that showed the highest build-up of O$_2$, while the biomimetic coenosarc areas were chosen in proximity to the polyp areas. For each profile, the diffusive O$_2$ flux was calculated using Fick's first law of diffusion as described previously[31] (using a diffusion coefficient of $D_{O2} = 2.2417 \times 10^{-5}$). The effective DBL thickness δe as the intersection between the extrapolation of the linear part of the O$_2$ slope within the boundary layer that intercepts with the O$_2$ concentration of the bulk medium was calculated.[75]

ROS Measurements: To investigate potential differences in ROS production by *B. psygmophilum* encapsulated on top of porous versus solid skeletons, H$_2$O$_2$ production was measured. H$_2$O$_2$ rapidly diffuses out of algal cells and is more easily measured compared to other ROS (e.g., singlet oxygen or superoxide) due to its longer lifetime.[76,77] Each bioprinted scaffold was incubated in 5 mL f/2 media in six-well plates at 25 °C and at a light intensity of 150 µmol m^{-2} s^{-1} photons for 40 min. Six replicate prints of each skeletal type were tested and for each print, 600 µL media was sampled for ROS analysis. Additionally, blank

samples of f/2 medium (incubated under identical conditions) were also sampled. As ROS diffuses out of the cells into the medium, the medium was quickly stirred with the pipette before sampling to ensure a homogeneous concentration of ROS in the medium.

H_2O_2 analysis was based on the reaction between H_2O_2 and the colorimetric probe Ampiflu™ Red (AR), which was catalyzed by horseradish peroxidase (HRP). Water samples were amended with AR (18 µmol L^{-1}) and HRP (0.4 kU L^{-1}) in a clear 96-well plate (final concentrations). Hydrogen peroxide standards were prepared from a primary stock solution made by diluting 30% hydrogen peroxide with ultrapure water, which was calibrated by measuring its absorbance at 240 nm and applying the molar extinction coefficient of hydrogen peroxide at this wavelength, which is 38.1 L mol^{-1} cm^{-1}.[78] Blanks were prepared with the addition of the hydrogen peroxide-degrading enzyme catalase (10 mg L^{-1}) to account for the autooxidation of AR. All chemicals were obtained from Millipore Sigma. Absorbance was measured at 530 and 700 nm (reference wavelength) using a SpectraMax M series multi-mode plate reader (Molecular Devices). All analysis was performed on reference-corrected data by subtracting the absorbance at 700 nm from the absorbance at 530 nm. The detection limit of hydrogen peroxide, defined as five times the standard deviation of replicate blank measurements, was 27 nM.

Mass Transfer and Fluid Flow Modeling: To quantify the DBL in silico, a computational model was built in the COMSOL Multiphysics.[79] The model was based on the experimental setup and consisted of a porous skeleton covered by a layer of O_2-producing tissue, placed in a tube with a laminar flow rate of 1 cm s^{-1}. The DBL is computed by combining COMSOLs physics interfaces "Transport of Diluted Species", "Transport of Diluted Species in Porous Media", and "Laminar Flow". The laminar flow was limited to the water and did not enter the model's tissue layer or skeleton. Diffusion of O_2 was modeled in both the water and the tissue layer, as well as in the skeleton if its porosity (V_{voids}/V_{total}) was set above zero. The diffusion constant of O_2 was assumed to be constant in all domains. The model was solved for different flow rates and porosities of the skeleton to study the effect of these parameters on the model's DBL and O_2 dynamics.

Image Analysis: For the structural similarity index, the µCT scanned scaffolds were binarized using an automated thresholding algorithm. Rigid registration was performed to align the 3D models of printed and native coral. A 3D binary structural similarity index was performed using *ssim*, to quantify the geometric similarity between the printed and native coral.[55] Due to inherent noise introduced during the µCT process and variations in signal intensity of the scaffold, this process did not perfectly approximate the internal and external borders of the coral scaffold. Manual segmentation was the gold standard for defining the borders of a construct. However, the µCT scans of these scaffolds were very large datasets (≈3000 × 3000 × 3000 voxels). Performing manual segmentation of these datasets was deemed unnecessary as the threshold-based structural similarity index values were deemed strong enough. Additionally, by visually comparing the 3D printed scaffold to the input 3D geometry (Figure 4F, Figure S11, Supporting Information), one could see that there was a high level of agreement between the two geometric structures. In situations where the input mask might only be a few µm across, there might be a loss of the finest features of the resultant printed scaffold due to a lack of structural stability of the feature during the 3D printing process.

Quantification of the number and size of microalgal aggregates imaged using confocal microscopy was accomplished using a custom-written macro on ImageJ. Stack of images were rendered to basic denoising, Gaussian filtering, and background subtraction prior to auto thresholding using the Li algorithm. The results were filtered with a minimum area of 50 $µm^2$ as well as a minimum value of 0.5 for circularity and roundness. As an individual aggregate could be detected across multiple adjacent slices in a z-stack, a Python code was used to group the values attributed to the same aggregate (Figure S12, Supporting Information). The cross-sectional areas detected in consecutive slices were categorized under the same aggregate if the x- and y-position of the area center were within the vicinity beneath a preset threshold. For

each aggregate, the maximum value was selected as the cross-sectional area.

Statistical Analysis: One-way analysis of variance (ANOVA) was used to test for significant differences in DBL thickness, O_2 flux, and ROS production between the different experimental treatments. Three-way ANOVA was used to test for statistical differences in algal aggregate size between oral and aboral tissues, in the presence of the gastric cavity and as a function of flow versus stagnant conditions. Statistical significance was assessed at a p-value of < 0.05. Bar charts represent means ±SD (unless otherwise indicated). Box charts show the mean, median, the 25% to 75% percentile as well as the range within the 1.5 interquartile range (IQR). All statistical analysis and data plotting was performed with Origin Pro 2021b (Origin, USA).

Supporting Information

Supporting Information is available from the Wiley Online Library or from the author.

Conflict of Interest

The authors declare no conflict of interest.

Data Availability Statement

The data that support the findings of this study are available in the supplementary material of this article.

[1] O. Hoegh-Guldberg, P. J. Mumby, A. J. Hooten, R. S. Steneck, P. Greenfield, E. Gomez, C. D. Harvell, P. F. Sale, A. J. Edwards, K. Caldeira, N. Knowlton, C. M. Eakin, R. Iglesias-Prieto, N. Muthiga, R. H. Bradbury, A. Dubi, M. E. Hatziolos, *Science* **2007**, *318*, 1737.

[2] J. Wiedenmann, C. D'Angelo, E. G. Smith, A. N. Hunt, F.-E. Legiret, A. D. Postle, E. P. Achterberg, *Nat. Clim. Change* **2013**, *3*, 160.

[3] T. P. Hughes, J. T. Kerry, M. Álvarez-Noriega, J. G. Álvarez-Romero, K. D. Anderson, A. H. Baird, R. C. Babcock, M. Beger, D. R. Bellwood, R. Berkelmans, T. C. Bridge, I. R. Butler, M. Byrne, N. E. Cantin, S. Comeau, S. R. Connolly, G. S. Cumming, S. J. Dalton, G. Diaz-Pulido, C. M. Eakin, W. F. Figueira, J. P. Gilmour, H. B. Harrison, S. F. Heron, A. S. Hoey, J.-P. A. Hobbs,

ADVANCED
SCIENCE NEWS
www.advancedsciencenews.com

ADVANCED
FUNCTIONAL
MATERIALS
www.afm-journal.de

M. O. Hoogenboom, E. V. Kennedy, C. Y. Kuo, J. M. Lough, et al., *Nature* **2017**, *543*, 373.

[4] B. E. Brown, *Coral Reefs* **1997**, *16*, S129.

[5] J. B. C. Jackson, *Science* **2001**, *293*, 629.

[6] T. P. Hughes, K. D. Anderson, S. R. Connolly, S. F. Heron, J. T. Kerry, J. M. Lough, A. H. Baird, J. K. Baum, M. L. Berumen, T. C. Bridge, D. C. Claar, C. M. Eakin, J. P. Gilmour, N. A. J. J. Graham, H. Harrison, J.-P. A. Hobbs, A. S. Hoey, M. Hoogenboom, R. J. Lowe, M. T. McCulloch, J. M. Pandolfi, M. Pratchett, V. Schoepf, G. Torda, S. K. Wilson, *Science* **2018**, *359*, 80.

[7] T. P. Hughes, A. H. Baird, D. R. Bellwood, M. Card, S. R. Connolly, C. Folke, R. Grosberg, O. Hoegh-Guldberg, J. B. C. Jackson, J. Kleypas, *Science* **2003**, *301*, 929.

[8] S. D. Donner, W. J. Skirving, C. M. Little, M. Oppenheimer, O. Hoegh-Guldberg, *Glob. Change Biol.* **2005**, *11*, 2251.

[9] O. Hoegh-Guldberg, *Mar. Freshwater Res.* **1999**, *50*, 839.

[10] L. M. Brander, P. Van Beukering, H. S. J. Cesar, *Ecol. Econ.* **2007**, *63*, 209.

[11] N. Pascal, M. Allenbach, A. Brathwaite, L. Burke, G. Le Port, E. Clua, *Ecosyst. Serv.* **2016**, *21*, 72.

[12] R. Costanza, R. de Groot, P. Sutton, S. van der Ploeg, S. J. Anderson, I. Kubiszewski, S. Farber, R. K. Turner, *Glob. Environ. Change* **2014**, *26*, 152.

[13] H. M. Putnam, *J. Exp. Biol.* **2021**, *224*, jeb239319.

[14] M. J. H. van Oppen, J. K. Oliver, H. M. Putnam, R. D. Gates, *Proc. Natl. Acad. Sci.* **2015**, *112*, 2307.

[15] J. A. van de Water, R. Tignat-Perrier, D. Allemand, C. Ferrier-Pagès, *Curr. Opin. Biotechnol.* **2022**, *74*, 110.

[16] P. Buerger, C. Alvarez-Roa, C. W. Coppin, S. L. Pearce, L. J. Chakravarti, J. G. Oakeshott, O. R. Edwards, M. J. H. van Oppen, *Sci. Adv.* **2020**, *6*, aba2498.

[17] S. K. Davy, D. Allemand, V. M. Weis, *Microbiol. Mol. Biol. Rev.* **2012**, *76*, 229.

[18] V. M. Weis, S. K. Davy, O. Hoegh-Guldberg, M. Rodriguez-Lanetty, J. R. Pringle, *Trends Ecol. Evol.* **2008**, *23*, 369.

[19] V. M. Weis, *Integr. Comp. Biol.* **2019**, *59*, 845.

[20] T. C. LaJeunesse, J. E. Parkinson, P. W. Gabrielson, H. J. Jeong, J. D. Reimer, C. R. Voolstra, S. R. Santos, *Curr. Biol.* **2018**, *28*, 2570.

[21] D. Bourne, Y. Iida, S. Uthicke, C. Smith-Keune, *ISME J.* **2008**, *2*, 350.

[22] T. D. Ainsworth, R. V. Thurber, R. D. Gates, *Trends Ecol. Evol.* **2010**, *25*, 233.

[23] D. Wangpraseurt, A. W. D. Larkum, P. J. Ralph, M. Kühl, *Front. Microbiol* **2012**, *3*, 316.

[24] N. Chindapol, J. A. Kaandorp, C. Cronemberger, T. Mass, A. Genin, *PLoS Comput. Biol.* **2013**, *9*, 1002849.

[25] S. Enríquez, E. R. Méndez, R. Iglesias-Prieto, *Limnol. Oceanogr.* **2005**, *50*, 1025.

[26] S. V. Murphy, A. Atala, *Nat. Biotechnol.* **2014**, *32*, 773.

[27] H. Kang, S. J. Lee, I. K. Ko, C. Kengla, J. J. Yoo, A. Atala, *Nat. Biotechnol.* **2016**, *34*, 312.

[28] M. Tang, Q. Xie, R. C. Gimple, Z. Zhong, T. Tam, J. Tian, R. L. Kidwell, Q. Wu, B. C. Prager, Z. Qiu, A. Yu, Z. Zhu, P. Mesci, H. Jing, J. Schimelman, P. Wang, D. Lee, M. H. Lorenzini, D. Dixit, L. Zhao, S. Bhargava, T. E. Miller, X. Wan, J. Tang, B. Sun, B. F. Cravatt, A. R. Muotri, S. Chen, J. N. Rich, *Cell Res.* **2020**, *30*, 833.

[29] P. Datta, M. Dey, Z. Ataie, D. Unutmaz, I. T. Ozbolat, *npj Precis. Oncol.* **2020**, *4*, 18.

[30] D. Wangpraseurt, S. You, Y. Sun, S. Chen, *Trends Biotechnol.* **2022**, https://doi.org/10.1016/j.tibtech.2022.01.003.

[31] D. Wangpraseurt, S. You, F. Azam, G. Jacucci, O. Gaidarenko, M. Hildebrand, M. Kühl, A. G. Smith, M. P. Davey, A. Smith, D. D. Deheyn, S. Chen, S. Vignolini, *Nat. Commun.* **2020**, *11*, 1748.

[32] H. H. Hwang, W. Zhu, G. Victorine, N. Lawrence, S. Chen, *Small Methods* **2018**, *2*, 1700277.

[33] C. A. Lawson, J. Raina, T. Kahlke, J. R. Seymour, D. J. Suggett, *Environ. Microbiol. Rep.* **2018**, *10*, 7.

[34] M. Kühl, Y. Cohen, T. Dalsgaard, B. B. Jørgensen, N. P. Revsbech, *Mar. Ecol.: Prog. Ser.* **1995**, *117*, 159.

[35] M. Omer, A. Carrasco-Pena, N. Orlovskaya, B. E. Collins, S. N. Yarmolenko, J. Sankar, G. Subhash, D. S. Gilliam, J. E. Fauth, *Adv. Appl. Ceram.* **2020**, *119*, 434.

[36] I. M. Jimenez, M. Kühl, A. W. D. Larkum, P. J. Ralph, *J. R. Soc., Interface* **2011**, *8*, 1785.

[37] H. M. Putnam, K. L. Barott, T. D. Ainsworth, R. D. Gates, *Curr. Biol.* **2017**, *27*, R528.

[38] T. Mass, A. Genin, U. Shavit, M. Grinstein, D. Tchernov, *Proc. Natl. Acad. Sci. USA* **2010**, *107*, 2527.

[39] D. De Beer, M. Kühl, N. Stambler, L. Vaki, *Mar. Ecol.: Prog. Ser.* **2000**, *194*, 75.

[40] M. Tresguerres, K. L. Barott, M. E. Barron, D. D. Deheyn, D. I. Kline, L. B. Linsmayer, in *Acid-Base Balance and Nitrogen Excretion in Invertebrates*, (Eds: D. Weihrauch, M. O'Donnell), Springer, Cham **2017**, p. 193.

[41] C. B. Bove, R. F. Whitehead, A. M. Szmant, *Coral Reefs* **2020**, *39*, 1675.

[42] D. M. Yost, L.-H. Wang, T.-Y. Fan, C.-S. Chen, R. W. Lee, E. Sogin, R. D. Gates, *Zool.* **2013**, *116*, 262.

[43] D. Wangpraseurt, M. Pernice, P. Guagliardo, M. R. Kilburn, P. L. Clode, L. Polerecky, M. Kühl, *ISME J.* **2015**, *10*, 788.

[44] J. Baier Leach, K. A. Bivens, C. W. Patrickjr, C. E. Schmidt, *Biotechnol. Bioeng.* **2003**, *82*, 578.

[45] W. Zhu, X. Qu, J. Zhu, X. Ma, S. Patel, J. Liu, P. Wang, C. S. E. Lai, M. Gou, Y. Xu, K. Zhang, S. Chen, *Biomaterials* **2017**, *124*, 106.

[46] D. Wangpraseurt, C. Wentzel, S. L. Jacques, M. Wagner, M. Kühl, *J. Roy. Soc., Interface* **2017**, *14*, 20161003 .

[47] D. Wangpraseurt, A. W. D. Larkum, J. Franklin, M. Szabo, P. J. Ralph, M. Kuhl, *J. Exp. Biol.* **2014**, *217*, 489.

[48] O. Levy, Z. Dubinsky, Y. Achituv, J. Erez, *J. Exp. Mar. Biol. Ecol.* **2006**, *333*, 1.

[49] O. Levy, Z. Dubinsky, Y. Achituv, *J. Exp. Biol.* **2003**, *206*, 4041.

[50] G. H. Yang, M. Yeo, Y. W. Koo, G. H. Kim, *Macromol. Biosci.* **2019**, *19*, 1800441.

[51] M. Pernice, J.-B. Raina, N. Rädecker, A. Cárdenas, C. Pogoreutz, C. R. Voolstra, *ISME J.* **2020**, *14*, 325.

[52] N. Kramer, J. G. , S. Chen, D. Wangpraseurt, Y. Loya, *biorxiv* **2021**, http://doi.org/10.1101/2021.09.29.462347

[53] C.-Y. Sun, C. A. Stifler, R. V. Chopdekar, C. A. Schmidt, G. Parida, V. Schoeppler, B. I. Fordyce, J. H. Brau, T. Mass, S. Tambutté, P. U. P. A. Gilbert, *Proc. Natl. Acad. Sci.* **2020**, *117*, 30159.

[54] H. H. Hwang, S. You, X. Ma, L. Kwe, G. Victorine, N. Lawrence, X. Wan, H. Shen, W. Zhu, S. Chen, *Biofabrication* **2020**, *13*, 025007.

[55] Z. Wang, A. C. Bovik, H. R. Sheikh, E. P. Simoncelli, *IEEE Trans. Image Process.* **2004**, *13*, 600.

[56] M. P. Lesser, C. D. Mobley, J. D. Hedley, M. Slattery, *Mar. Ecol.: Prog. Ser.* **2021**, *670*, 49.

[57] D. Jamieson, B. Chance, E. Cadenas, A. Boveris, *Annu. Rev. Physiol.* **1986**, *48*, 703.

[58] H. I. Albalawi, Z. N. Khan, A. U. Valle-Pérez, K. M. Kahin, M. Hountondji, H. Alwazani, S. Schmidt-Roach, P. Bilalis, M. Aranda, C. M. Duarte, C. A. E. Hauser, *ACS Sustainable Chem. Eng.* **2021**, *9*, 12634.

[59] N. Levy, O. Berman, M. Yuval, Y. Loya, T. Treibitz, E. Tarazi, O. Levy, *Sci. Total Environ.* **2022**, *830*, 154749.

[60] M. Weber, D. de Beer, C. Lott, L. Polerecky, K. Kohls, R. M. M. Abed, T. G. Ferdelman, K. E. Fabricius, *Proc. Natl. Acad. Sci.* **2012**, *109*, E1558.

[61] N. C. S. Chan, D. Wangpraseurt, M. Kühl, S. R. Connolly, *Front. Mar. Sci.* **2016**, *3*, https://doi.org/10.3389/fmars.2016.00010.

[62] B. B. Jørgensen, D. J. Des Marais, *Limnol. Oceanogr.* **1990**, *35*, 1343.

[63] H. Røy, M. Hüttel, B. B. Jørgensen, *Limnol. Oceanogr.* **2002**, *47*, 837.

[64] W. Zhu, K. R. Tringale, S. A. Woller, S. You, S. Johnson, H. Shen, J. Schimelman, M. Whitney, J. Steinauer, W. Xu, T. L. Yaksh, Q. T. Nguyen, S. Chen, *Mater. Today* **2018**, *21*, 951.

[65] R. R. L. Guillard, J. H. Ryther, *Can. J. Microbiol.* **1962**, *8*, 229.

[66] M. Polne-Fuller, *J. Phycol.* **1991**, *27*, 552.

[67] L. M. Roger, H. G. Reich, E. Lawrence, S. Li, W. Vizgaudis, N. Brenner, L. Kumar, J. Klein-Seetharaman, J. Yang, H. M. Putnam, N. A. Lewinski, *PLoS One* **2021**, *16*, 0248953.

[68] Y. Fang, J. Tan, S. Lim, S. Soh, *NPG Asia Mater* **2018**, *10*, 465.

[69] O. Jeon, K. H. Bouhadir, J. M. Mansour, E. Alsberg, *Biomaterials* **2009**, *30*, 2724.

[70] J. W. Nichol, S. T. Koshy, H. Bae, C. M. Hwang, S. Yamanlar, A. Khademhosseini, *Biomaterials* **2010**, *31*, 5536.

[71] B. D. Fairbanks, M. P. Schwartz, C. N. Bowman, K. S. Anseth, *Biomaterials* **2009**, *30*, 6702.

[72] C. Yu, K. L. Miller, J. Schimelman, P. Wang, W. Zhu, X. Ma, M. Tang, S. You, D. Lakshmipathy, F. He, S. Chen, *Biomaterials* **2020**, *258*, 120294.

[73] J. L. Drake, T. Mass, L. Haramaty, E. Zelzion, D. Bhattacharya, P. G. Falkowski, *Proc. Natl. Acad. Sci.* **2013**, *110*, 3788.

[74] K. E. Brodersen, M. Lichtenberg, P. J. Ralph, M. Kühl, D. Wangpraseurt, *J. R. Soc., Interface* **2014**, *11*, 20130997.

[75] B. B. Jørgensen, N. P. Revsbech, *Limnol. Oceanogr.* **1985**, *30*, 111.

[76] Y. Shaked, R. Armoza-Zvuloni, *J. Geophys. Res.: Biogeosci.* **2013**, *118*, 1793.

[77] J. M. Diaz, C. M. Hansel, A. Apprill, C. Brighi, T. Zhang, L. Weber, S. McNally, L. Xun, *Nat. Commun.* **2016**, *7*, 13801.

[78] W. L. Miller, D. R. Kester, *Anal. Chem.* **1988**, *60*, 2711.

[79] *COMSOL Multiphysics v. 5.6., COMSOL AB Stockholm*, Sweden, www.comsol.com.